Kinetic, Spectroscopic, and X-ray Crystallographic Characterization of the Functional E151H Aminopeptidase from *Aeromonas proteolytica*[†,‡]

Krzysztof P. Bzymek,[§] Aaron Moulin,[||] Sabina I. Swierczek,[§] Dagmar Ringe,*[,||] Gregory A. Petsko,*[,||] Brian Bennett,*[,⊥] and Richard C. Holz*[,§]

Department of Chemistry and Biochemistry, Utah State University, Logan, Utah 84322-0300, the Program in Biophysics and Structural Biology, Departments of Biochemistry and Chemistry and the Rosenstiel Basic Medical Sciences Research Center, Brandeis University, 415 South Street, Waltham, Massachusetts 02254, and the National Biomedical EPR Center, Department of Biophysics, Medical College of Wisconsin, Milwaukee, Wisconsin 53226-0509

Received March 30, 2005; Revised Manuscript Received July 11, 2005

ABSTRACT: Glutamate151 (E151) has been shown to be catalytically essential for the aminopeptidase from *Vibrio proteolyticus* (AAP). E151 acts as the general acid/base during the catalytic mechanism of peptide hydrolysis. However, a glutamate residue is not the only residue capable of functioning as a general acid/base during catalysis for dinuclear metallohydrolases. Recent crystallographic characterization of the D-aminopeptidase from *Bacillus subtilis* (DppA) revealed a histidine residue that resides in an identical position to E151 in AAP. Because the active-site ligands for DppA and AAP are identical, AAP has been used as a model enzyme to understand the mechanistic role of H115 in DppA. Substitution of E151 with histidine resulted in an active AAP enzyme exhibiting a k_{cat} value of 2.0 min^{-1}, which is over 2000 times slower than r AAP (4380 min^{-1}). ITC experiments revealed that Zn^{II} binds 330 and 3 times more weakly to E151H-AAP compared to r-AAP. UV−vis and EPR spectra of Co^{II}-loaded E151H-AAP indicated that the first metal ion resides in a hexacoordinate/pentacoordinate equilibrium environment, whereas the second metal ion is six-coordinate. pH dependence of the kinetic parameters k_{cat} and K_m for the hydrolysis of L-leucine *p*-nitroanilide (L-*p*NA) revealed a change in an ionization constant in the enzyme−substrate complex from 5.3 in r-AAP to 6.4 in E151H-AAP, consistent with E151 in AAP being the active-site general acid/base. Proton inventory studies at pH 8.50 indicate the transfer of one proton in the rate-limiting step of the reaction. Moreover, the X-ray crystal structure of [ZnZn(E151H-AAP)] has been solved to 1.9 Å resolution, and alteration of E151 to histidine does not introduce any major conformational changes to the overall protein structure or the dinuclear Zn^{II} active site. Therefore, a histidine residue can function as the general acid/base in hydrolysis reactions of peptides and, through analogy of the role of E151 in AAP, H115 in DppA likely shuttles a proton to the leaving group of the substrate.

Metalloproteases that contain cocatalytic metallo-active sites are key players in numerous biological processes, including but not limited to tissue repair, angiogenesis, neurological processes, protein maturation and degradation, hormone level regulation, cell-cycle control, and bacterial antibiotic resistance (*1*−*6*). The importance of understanding the mechanism of action of these metalloproteases is underscored by their central role in disease states that include stroke, diabetes, cancer, HIV, bacterial infections, and neuropsychiatric disorders associated with the dysregulation of glutamatergic neurotransmission, such as schizophrenia, seizure disorders, and amyotrophic lateral sclerosis (ALS) (*1*, *2*, *7*−*11*). For example, the naturally occurring peptide analogue inhibitor, bestatin, was shown to significantly decrease HIV infection in males by inhibiting leucine aminopeptidase activity (*12*). Moreover, a recent study has shown that several naturally occurring aminopeptidase inhibitors (i.e., bestatin, leuhistin, and actinonin) inhibit matrix degradation and invasion of extracellular matrixes by fibrosarcoma cells (*13*). For these reasons, several metallopeptidases that contain cocatalytic active sites have become the subject of intense efforts in inhibitor design (*1*, *14*−*18*).

Different classification systems exist for metallopeptidases that include parameters such as enzymatic properties (catalytic function, molecular weight, pH optimum, requirement

[†] This work was supported by the National Science Foundation (CHE-02408102, to R.C.H.), the Medical College of Wisconsin Research Affairs Committee (to B.B.), the National Institutes of Health (GM26788, to G.A.P. and D.R.) and, in part, by the Macromolecular Structure and Mechanisms Training Grant from NIH (CCS). The Bruker ESP-300E EPR spectrometer was purchased with funds provided by the National Science Foundation (BIR-9413530), and XSophe was purchased with funds from the National Institutes of Health (NIH RR01008, to B.B.)

[‡] The coordinates have been deposited in the Protein Data Bank and are available under access code 2ANP.

* To whom correspondence should be addressed: Department of Chemistry and Biochemistry, Utah State University, Logan, UT 84322-0300. Telephone: (435) 797-2609. Fax: (435) 797-3390, E-mail: rholz@cc.usu.edu (R.C.H.); Departments of Biochemistry and Chemistry and the Rosenstiel Basic Medical Sciences Research Center, Brandeis University, Waltham, MA 02254. Telephone: (781) 736-4905. Fax: (781) 736-2405. E-mail: petsko@brandeis.edu (G.A.P.).

[§] Utah State University.

[||] Brandeis University.

[⊥] Medical College of Wisconsin.

10.1021/bi0505823 CCC: $30.25
Published on Web 08/19/2005

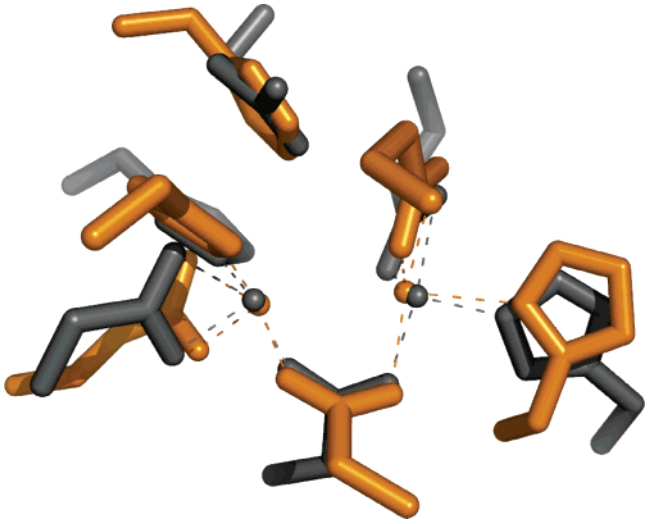

FIGURE 1: Superposition of the active sites of APP (gray; PDB 1AMP) and DppA (gold; PDB 1HI9).

for cofactors, etc.), cellular location, and peptide sequence similarity (*19*). In the proposed catalytic mechanisms of most metallopeptidases, a glutamate moiety is utilized to activate a metal-coordinated water molecule and also acts as a general acid/base (*20*−*22*). However, in the X-ray crystal structure of the D-aminopeptidase from *Bacillus subtilis* (DppA),[1] a member of the dipeptide transport protein family, an active-site histidine residue (H115) replaces the glutamate residue (E151) that acts as the general acid/base in the crystallographically characterized aminopeptidase from *Aeromonas proteolytica* (AAP) (*22*−*24*). Because the cocatalytic metallo-active sites of AAP and DppA contain an identical set of metal ligands (Figure 1), H115 of DppA was proposed to function as the general acid/base (*22*−*24*). The cellular role of DppA is currently unknown; it is the first product of the *dpp* operon expressed early in sporulation (*25*). The fact that DppA specifically acts on D-amino acids (D-Ala-D-Ala and D-Ala-Gly-Gly) suggests its involvement in the degradation of amino acids used in peptidoglycan synthesis (*26*). Enzymes in the biosynthetic pathway of peptidoglycan, e.g., *N*-succinyl-L,L-diaminopimelic acid desuccinylase (DapE) and *N*-acetyl-L-ornithine deacetylase (ArgE), are promising targets of antibacterial agents (*1*, *27*, *28*). The first discovered antibiotic and still most widely prescribed, penicillin, affects the cross-linking reactions of peptidoglycan binding to transpeptidases. In this context, understanding of the role of DppA as well as its mechanism of action is of great importance in the fight against the growing bacterial resistance to known antibiotics.

AAP, while not a specific pharmaceutical target at this time, is one of the best mechanistically characterized metallopeptidase containing a cocatalytic metallo-active site (*1*, *29*). Because the large majority of cocatalytic metallopeptidases contain active sites that are identical to that observed in AAP, the major steps of their catalytic mechanisms will likely be similar. Recent studies on the mechanistic role of an active-site glutamate residue (E151) in AAP revealed that it functions as the general acid/base (*22*). Therefore, we have substituted E151 in AAP with a histidine residue (E151H-AAP) as a model for DppA. Interestingly, E151H-AAP is active toward L-leucine-*p*-nitroanalide; therefore, the enzyme was characterized by kinetic methods. In an effort to gain insight into the role of H115 in the hydrolysis of D-amino acids by DppA, we have used both spectroscopic and crystallographic methods to examine the structure of E151H-AAP. The spectroscopic and X-ray crystallographic data presented herein combined with the previously reported mechanistic data for AAP (*29*) also provide additional insight into the role of E151 in the catalytic mechanism of peptide hydrolysis.

MATERIALS AND METHODS

Mutagenesis and Enzyme Purification. All chemicals used in this study were purchased from commercial sources and were of the highest quality available. The plasmid encoding for the 51 kDa form of AAP (pVSNMC) was a generous gift from Prof. Kiyoshi Hayashi (*30*). E151H-AAP was obtained by PCR mutagenesis using the following primers: 5′-GGC TTA TGC CGC TCA CGA AGT CGG CTT GCG-3′ and 5′-CGC AAG CCG ACT TCG TGA GCG GCA TAA GCC-3′ (MWG Biotech, High Point, NC). The PCR cycling parameters, plasmid isolation, transformation into *Escherichia coli* BL21 Star(DE3) (Invitrogen, Carlsbad, CA), and growth conditions are described elsewhere (*22*). E151H-AAP was purified according to the previously published procedure with only minor modifications in the heat treatment step. Briefly, a starter culture was grown in sterile Luria−Bertani (LB) medium at 37 °C until an OD_{600} of 0.6−0.8 was obtained. This culture was then used to inoculate a 5 L fermentor (New Brunswick, Edison, NJ) containing sterile LB medium. The bacteria were grown at 37 °C with aeration until an OD_{600} of 1.2 was reached. At this point, the temperature was lowered to 25 °C followed by the addition of 1.2 g of isopropyl-*β*-D-thiogalactopyranoside (IPTG) and the bacteria were allowed to grow for 12−16 h. The cells were then harvested by centrifugation using a Beckman Avanti J-25 centrifuge (8000 rpm, 15 min, 4 °C). The supernatant, after centrifugation (containing LB broth and the protein), was saturated with ammonium sulfate. The precipitate was collected by centrifugation at 10 000 rpm for 45 min at 4 °C. The pellet, containing E151H-AAP, was resuspended in 30 mL of 10 mM *N*-tris[hydroxymethyl]-methylglycine (Tricine) buffer (pH 8.0) containing 0.1 mM Zn^{II}. This protein solution was dialyzed overnight against 4 L of the same buffer. The crude supernatant, containing the protein after dialysis, was treated with proteinase K at 37 °C. The activity of E151H-AAP toward L-leucine-*p*-nitroanilide (L-*p*NA) was monitored every 5 min, and when the activity did not change after two consecutive measurements, the enzyme solution was heated at 50 °C, until no further changes in activity were observed. The enzyme was then concentrated in an Amicon stirred cell containing a YM10 membrane (Millipore Corp., Bedford, MA) to 5−10 mL, and NaCl was added to a final concentration of 1 M. This enzyme

[1] Abbreviations: AAP, leucine aminopeptidase from *Aeromonas proteolytica* (*Vibrio proteolyticus*); rAAP, recombinant leucine aminopeptidase; ArgE, *N*-acetyl-L-ornithine deacetylase; DapE, *N*-succinyl-L,L-diaminopimelic acid desuccinylase; DppA, D-aminopeptidase from *Bacillus subtilis*; EPR, electron paramagnetic resonance; HEPES, 4-(2-hydroxyethyl)-1-piperazineethanesulfonic acid; ICP−AES, inductively coupled plasma−atomic emission spectroscopy; IPTG, isopropyl-*β*-D-thiogalactopyranoside; ITC, isothermal titration calorimetry; LB, Luria−Bertani; L-*p*NA, L-leucine-*p*-nitroanilide; Tricine, *N*-tris[hydroxymethyl]-methylglycine; SDS−PAGE, sodium dodecyl sulfate−polyacrylamide gel electrophoresis; WT, wild type.

solution was applied to an Octyl-Sepharose column (3 × 30 cm) (Amersham Biosciences Corp., Piscataway, NJ) that had been pre-equilibrated with 10 mM Tricine buffer at pH 8.0, 1 M NaCl, and 0.1 mM $ZnSO_4$. E151H-AAP was eluted with 10 mM Tricine buffer at pH 8.0 containing 0.1 mM $ZnSO_4$. The pooled fractions containing the E151H-AAP enzyme were concentrated in an Amicon stirred cell. To remove any additional pigment associated with the protein derived from LB broth, a second purification step was employed that involved applying the E151H-AAP sample to a Fast Flow Q-Sepharose column (Amersham Biosciences Corp., Piscataway, NJ) (3 × 30 cm) pre-equilibrated with 10 mM Tricine buffer at pH 8.0 and 0.1 mM $ZnSO_4$. E151H-AAP was eluted with a 0−1 M NaCl gradient. All purification steps were carried out at 4 °C, and the purity of each final protein sample was confirmed by sodium dodecyl sulfate−polyacrylamide gel electrophoresis (SDS−PAGE).

Enzymatic Assay. E151H-AAP was assayed for catalytic activity with L-*p*NA as the substrate (*31*). In this assay, the hydrolysis of L-*p*NA was measured spectrophotometrically by monitoring the formation of *p*-nitroaniline at 405 nm (ϵ = 10 800 M^{-1} cm^{-1}) in a cell with a 1 cm path length. All assays were performed on a Shimadzu UV-3101PC spectrophotometer equipped with a constant-temperature cell holder and an Isotemp 2013D water bath (Fisher Scientific, Pittsburgh, PA). Enzyme concentrations were determined from the absorbance at 280 nm with the value ϵ_{280} = 43 950 M^{-1} cm^{-1} (*32*). All assays were performed at 25.0 ± 0.1 °C unless stated otherwise. All experiments were carried out in 10 mM potassium borate buffer at pH 8.0, unless stated otherwise.

pH Profiles. The enzymatic activity of E151H-AAP at pH values between 5.5 and 10.75 were measured using L-*p*NA as the substrate. The following buffers were used: carbonate (pH 10.75−10.50), borate (pH 8.00−10.50), phosphate (pH 8.00−6.50), and acetate (pH 6.00−5.50). Constant ionic strength was ensured by the presence of 0.2 M KCl in each assay. Because of Zn^{II} precipitation at higher pH values in phosphate buffers, the only source of Zn^{II} in the pH range of 6.50−10.75 was that previously added to the enzyme during purification. It has been shown that no significant Zn^{II} depletion occurs at pH values higher than 8.00 (*33*). To determine if Zn^{II} depletion occurs in phosphate buffers between pH 6.50 and 8.00, specific activity was measured versus enzyme/buffer incubation time. The observed activity did not decrease upon prolonged incubation of the E151H-AAP enzyme in Zn^{II}-free buffer; thus, the kinetic parameters should not be greatly affected by Zn^{II} depletion in this pH range. At pH 6.00, acetate buffer was used, which contained 10 mM Zn^{II} sulfate to prevent Zn^{II} depletion. Additionally, at pH 5.50, kinetic parameters were obtained from reciprocal plots of $1/k_{cat}$ versus 1/[Zn] and $1/K_m$ versus 1/[Zn] by extrapolation of the kinetic parameters to saturating Zn^{II} concentrations, as described in detail by Baker and Prescott (*33*). The kinetic parameters k_{cat}, K_m, and k_{cat}/K_m were determined using 9−10 different substrate concentrations in the range of 0.2−10.0 K_m at each pH value. Kinetic parameters and pH dependence fits were obtained using Igor Pro (Wavemetrix, Inc., Lake Oswego, OR) and SigmaPlot (SPSS, Inc., Chicago, IL) by fitting the experimental data to the appropriate equations.

Solvent Isotope Effect. All buffers were prepared in 99.9% [^{2}H] H_2O from a freshly opened bottle (Aldrich). Buffers with the desired atom fraction of deuterium were prepared by combining appropriate volumes of buffers made in H_2O and D_2O. The pH of each buffer used was adjusted using NaOD or DCl (both 99%+ deuterium content; Acros Organics, Geel, Belgium) and corrected for deuteration by adding 0.4 to the nominal pH reading of the pH meter. The buffer (10 mM potassium borate at pH 8.50) was prepared from the anhydrous salt and did not contain any Zn^{II} salts as zinc hydroxide/borate precipitates under these conditions.

Apoenzyme Preparation. Purified and concentrated E151H-AAP (approximately 20 mg/mL) was incubated with 10−15 mM disodium EDTA at 4 °C until no activity was observed (usually 1−3 days). To remove EDTA, the protein was dialyzed extensively against 100 times the volume of chelexed 50 mM 4-(2-hydroxyethyl)-1-piperazineethanesulfonic acid (HEPES) buffer at pH 7.5. The metal content was determined by inductively coupled plasma−atomic emission spectroscopy (ICP−AES) (Department of Agriculture, USU); zinc content in the protein was found to be less than 1%. All plasticware used for dialysis and the dialysis tubing were presoaked in a disodium-EDTA/bicarbonate solution to remove traces of metals and then extensively washed with Nanopure water (NANOpure Ultrapure Water System, Barnstead/Thermolyne, IA) and chelexed HEPES buffer.

Isothermal Titration Calorimetry (ITC). ITC measurements were carried out on a MicroCal OMEGA ultrasensitive titration calorimeter (MicroCal, Inc., Northampton, MA). The titrant ($CoCl_2$, 99.999%, and $ZnCl_2$, 99.999%, Acros Organics and Aldrich, respectively) and sample solution of apoprotein were prepared in chelexed 50 mM HEPES buffer at pH 7.5 and degassed prior to the experiment. The binding constant of Tricine to apo-E151H-AAP was also measured using a Tricine solution (50 mM) prepared in chelexed HEPES buffer. The pH of the resulting solution was adjusted to 7.5, and the binding constant for Zn^{II}-reconstituted E151H-AAP was determined using identical conditions to the metal-binding experiments. In a typical experiment, the enzyme (70 μM) was placed in the calorimeter cell and stirred at 200 rpm to ensure rapid mixing. Typically, 4−10 μL of the titrant was delivered over 7.6 s with 7-min intervals between injections to allow for complete equilibration. Each titration was continued until 3−6 equiv of the titrant had been added to ensure that no complexes formed in excess titrant. All titrant solutions for the determination of metal-binding constants were prepared in the same buffer as the protein to avoid any heat of dilution or metal complexation. A background titration, consisting of the identical titrant solution but only the buffer solution in the sample cell, was subtracted from each experimental titration to account for the heat of dilution. The data were analyzed using a Windows-based Origin software package supplied by MicroCal.

Spectroscopic Measurements. Electronic absorption spectra were recorded on a Shimadzu UV-3101PC spectrophotometer, and all solutions were degassed prior to performing an experiment. Apo-E151H-AAP (typically 0.3−1.2 mM) was incubated with Co^{II} ($CoCl_2$, ≥99.999%, Acros Organics, Geel, Belgium) for ∼10 min at 25 °C before a spectrum was recorded. Apoprotein absorbance was subtracted from

spectra obtained with Co^{II} using IgorPro (Wavemetrix, Inc., Lake Oswego, OR). Electron paramagnetic resonance (EPR) spectra were recorded using a Bruker ESP-300E instrument with an ER 4116 DM TE_{102}/TE_{012} dual-mode X-band cavity and an Oxford Instruments ESR-900 helium flow cryostat. All spectra were recorded at a modulation frequency of 100 kHz and a modulation amplitude of 12.6 G (1.26 mT). Protein concentrations used for the experiment were approximately 1 mM. Exact microwave frequencies and temperatures for individual spectra are provided in the figure captions. Computer simulations of EPR spectra were carried out using Xsophe version 1.1.2 (Bruker Biospin GmbH, Rheinstetten, Germany) (*34*). Parameters were fit to the spin Hamiltonian

$$H = \beta gHS + SDS + SAI \quad (1)$$

Under this formalism, $D > 0$ corresponds to a $M_S = |\pm^1/_2\rangle$ ground state and $D < 0$ corresponds to an $M_S = |\pm^3/_2\rangle$ ground state.

Crystallization. E151H-AAP was crystallized using the crystallization conditions reported for the native enzyme (*35*). Briefly, purified E151H-AAP (15 mg/mL) in 10 mM HEPES at pH 7.2, 10 mM KSCN, and 0.4 M NaCl was crystallized by vapor diffusion using 100 mM HEPES at pH 7.2, 100 mM KSCN, and 4.5 M NaCl as the precipitating solution. E151H-AAP crystals with dimensions 0.5 × 0.5 × 0.3 mm were obtained in 2−3 days and had identical morphology to wild-type (WT) crystals. The crystals belong to space group $P6_122$ with the following until cell dimensions: $a = b = 109.6$ Å, $c = 91.3$ Å, $\alpha = \beta = 90°$, and $\gamma = 120°$. There is one monomer per asymmetric unit.

Data Collection and Processing. Diffraction data were collected at room temperature (25 K) on an in-house source consisting of a Rigaku RU-300 rotating anode (copper anode) and a *R*-axis IV detector. Crystals were mounted into quartz capillaries directly from the drop. Molding putty was used to stabilize the capillary and mount it to the goniometer head. One crystal was used for the entire data collection period. Exposure times were 15 min, and the oscillation range was 0.75°. The beam size was 0.1 mm, and the crystal−detector distance was 110 mm. The diffraction data were integrated and scaled using Denzo and Scalepack (*36*). Data Collection and refinement statistics are provided in Table 1. It should be noted that here a resolution cutoff at $I/\sigma = 2.8$ was chosen. This is generally not practiced, and a resolution cutoff with $I/\sigma = 2.0$ is preferred. However, because of beam incoherency and limitation with the in-house detector diffraction fell off sharply at a resolution higher than 1.9 Å, falling to $I/\sigma = 1.2$ with an increase in R_{merge} to values greater than 80%. Hence, the choice was made to include only data at a resolution of 1.90 Å.

Structure Solution and Refinement. Phases were derived from a previously solved structure (PDB accession code 1AMP) in which the native glutamate residue in position 151 was replaced by an alanine residue. In this process, water molecules were omitted from the original coordinate file. All refinement procedures were carried out using the software package CNS (*37*). A R_{free} data set was made prior to any refinement using 10% of the total reflections. The initial model was subjected to a rigid-body refinement using all reflections in the 50.0−3.5 Å resolution range. After one round of rigid-body refinement with 20 cycles of refinement, the *R* factor and R_{free} were 32.5 and 33.5%, respectively. Because of the marked length change in the *c* axis (greater than 6 Å), a second round of rigid-body refinement was carried out to place the monomer better within the density. After this second round of rigid-body refinement, the *R* factor and R_{free} were 24.4 and 25.3%, respectively. After the second round of rigid-body refinement, one round each of simulated annealing, coordinate energy minimization and *B*-factor refinement were carried out. The *R* factor and R_{free} at this point were 23.0 and 25.3%, respectively, for E151H-AAP (*38*). Electron-density maps with amplitudes $2F_{obs} - F_{calc}$ and $F_{obs} - F_{calc}$ were then calculated and showed clear electron density in the active site for a histidine residue at position 151 (rather than the alanine residue contained in the starting model). At this point, a histidine residue was modeled into the density at position 151 in place of the alanine using O (*40*). Subsequent manual manipulations of all atomic models were performed in O. The model at this point was subjected to positional refinement and individual *B*-factor refinement. Electron-density maps were calculated, and manual repositioning of residues was performed. Water molecules were added to the model using the WATERPICK protocol in the CNS program. After the first round of water picking, the *R* factor and R_{free} were 20.8 and 23.5%, respectively. A sodium ion was added at this point in the refinement; it was judged to be a sodium ion because of an obvious octahedral arrangement of waters and protein-derived hydroxyl groups. Further rounds of positional refinement as well as individual *B*-factor refinement protocols were performed always followed by map calculation and manual repositioning of residues. After these refinements and an

Table 1: Data Collection and Refinement Statistics

crystal data	
space group	$P6_122$
unit cell parameters (Å)	$a = 106.9$
	$b = 106.9$
	$c = 91.3$
data processing	
number reflections, observed	457 444
number reflections, unique	27 824
cuttoff (I/σ)	2.8
R_{merge}[a] (overall) (%)	10.5
completeness, overall (%)	98.4
highest resolution shell (Å)	1.97−1.90
R_{merge}[a] (outer shell) (%)	56.6
completeness, outer shell (%)	99.3
overall I/σ	20.6
model refinement	
resolution range (Å)	50.0−1.9
cuttoff ($F/\sigma F$)	0
R factor[b] (%)	18.0
R_{free} (for 2624 reflections; %)	20.5
number of reflections	23 654
number of protein atoms	2212
number of zinc ions	2
number of water molecules	151
B factor model	individual
rmsd from ideality	
bond lengths (Å)	0.004
bond angles (deg)	1.19
improper angles (deg)	0.76
dihedral angles (deg)	22.8
residues in most favored positions[c] (%)	84.0
residues in disallowed regions (%)	0.0

[a] $R_{merge} = \sum|I_{obs} - I_{avg}|/\sum I_{avg}|$. [b] *R* factor $= \sum|F_{obs} - F_{calc}|/\sum|F_{obs}|$. [c] As determined by PROCHECK.

additional round of water picking, the final structure had reached a *R* factor of 18.0% and a R_{free} of 20.5%.

RESULTS

Kinetic Properties of E151H-AAP. The kinetic properties of E151H-AAP were initially determined in 10 mM Tricine buffer at pH 8.0 containing 0.1 mM $ZnSO_4$. A K_m value of 49.2 μM toward L-*p*NA was determined, which is ~5 times higher than that observed for r AAP (*20*). Because we suspected the increased K_m to be the result of Tricine inhibition, an inorganic borate buffer was used for further experiments. In 10 mM borate at pH 8.50 containing 0.2 M KCl, the K_m values for recombinant leucine aminopeptidase (rAAP), E151D-AAP, and E151H-AAP were very similar (16.4, 22.9, and 25.5 μM, respectively). The turnover number, k_{cat}, was 2.0 min^{-1}, nearly identical to that of E151D-AAP (2.4 min^{-1}) and 2200 times lower than that of AAP (k_{cat} = 4380 min^{-1}) (*22*).

ITC. ITC experiments were conducted on apo-E151H-AAP to determine the metal dissociation constants (K_d) (parts A and B of Figure 2). The heat of reaction, measured during the experiment, is converted into association constants (K_a) using the Gibbs free-energy relationship

$$\Delta G^\circ = -RT \ln(K_a) = \Delta H^\circ - T\Delta S^\circ \qquad (2)$$

where R = 1.9872 cal mol^{-1} K^{-1}. The relationship between K_a and K_d is defined as

$$K_d = 1/K_a \qquad (3)$$

For each measurement, the background heat of dilution was subtracted and K_a values were obtained by fitting these data via an iterative process using the Origin software package. The equilibrium binding constant, the enzyme−metal stoichiometry (*n*), and the change in enthalpy (ΔH) were allowed to vary during the fitting process (Table 2). The best fit was obtained using a model for two noninteracting sites (n = 2) (bottom panel in parts A and B of Figure 2). The K_d values obtained for Zn^{II} binding to E151H-AAP were 1.0 and 940 μM, for the first and second metal-binding events, respectively, which are 330 and 3 times weaker than WT-AAP. On the other hand, the K_d values obtained for Co^{II} binding to E151H-AAP were ~120- and ~5000-fold weaker for the first and second binding sites, respectively, versus r AAP. In addition, ITC experiments revealed that two Tricine molecules weakly interact with Zn^{II}-loaded E151H-AAP with K_d values of 5.2 and 26.9 mM, respectively. These values are similar to those observed for Tricine binding by Zn^{II}-loaded r AAP (K_{d_1} = 4.6 mM and K_{d_2} = 13.9 mM) (*24*).

pH Dependence. To further characterize the role of H151 in the catalytic mechanism of peptide hydrolysis, the kinetic parameters K_m, k_{cat}, and k_{cat}/K_m were recorded as a function of pH (Figure 3). The obtained kinetic data were plotted as log(parameter) versus pH and fit to eq 4

$$\text{parameter} = c/(1 + [H^+]/K_1 + K_2/[H^+]) \qquad (4)$$

where parameter is k_{cat} or k_{cat}/K_m and K_1 and K_2 are the respective ionization constants, while $[H^+]$ is the hydrogen ion concentration in solution. The observed changes in k_{cat} are small over the pH range of 7.5−9.5, but a sharp drop is

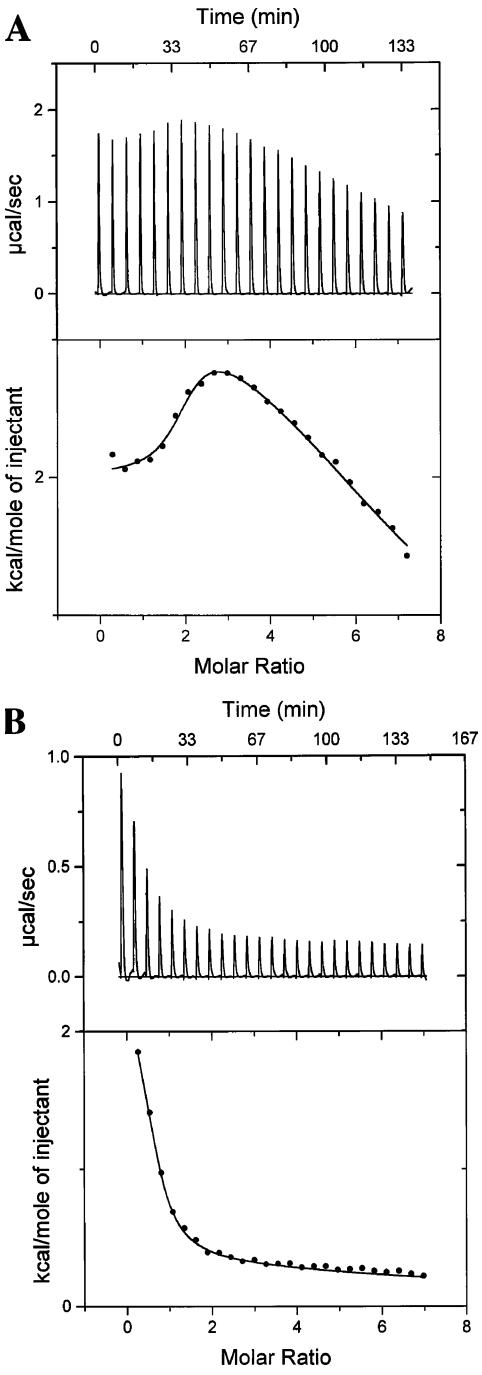

FIGURE 2: Isothermal titration data for the titration of apo-E151H-AAP with Zn^{II} (A) and Co^{II} (B) in 50 mM HEPES buffer at pH 7.5 and 25 °C.

observed below pH 7.5 with a single inflection at 6.4. A smaller drop is observed on the basic limb, with an apparent ionization at 11.2 (Figure 3B). The plot of log(k_{cat}/K_m) versus pH reveals one inflection in the acidic range, at 7.6, similar to the ionization constant of the substrate (7.7) (*33*) and one in the basic range at 10.8, which on the basis of previous studies was assigned to Y225 (Figure 3C) (*22*). The solid line in log K_m versus pH (Figure 3A) was obtained by subtracting the theoretical plots of log k_{cat}/K_m from log k_{cat} obtained using eq 4; thus, the inflection points reflect groups with ionizations at 6.4, 7.6, 10.8, and 11.2.

To determine the identity of the ionizing group exhibiting a pK_a of 6.4, the temperature dependence of k_{cat} was determined at saturating concentrations of substrate (4.5 mM)

Table 2: Metal-Binding Constants and Thermodynamic Parameters for Co^{II} and Zn^{II} Binding to Apo-E151H-AAP

	n	K_1, K_2 (M^{-1})	ΔH_1, ΔH_2 (kcal mol^{-1})	$T\Delta S_1$, $T\Delta S_2$ (kcal mol^{-1})	ΔG_1, ΔG_2 (kcal mol^{-1})
[ZnZn(E151H)]	1.08	9.62×10^5	2.01	10.17	−8.16
	1.10	1.06×10^3	3.94	8.07	−4.13
[CoCo(E151H)]	1.00	8.89×10^4	2.53	9.28	−6.75
	1.15	575	8.39	12.15	−3.76
[ZnZn(rAAP)]	1.21	3.19×10^8	1.36	12.95	−11.59
	1.05	3.93×10^3	5.23	10.14	−4.91
[CoCo(rAAP)]	0.97	1.06×10^7	0.21	9.71	−9.50
	0.90	2.77×10^6	10.03	18.45	−8.42

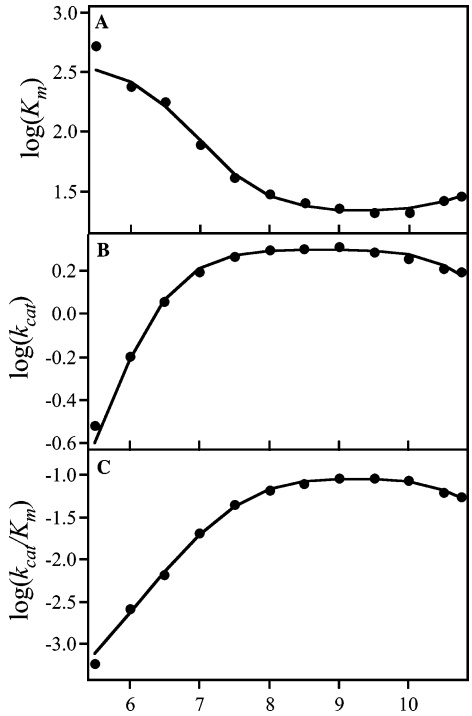

FIGURE 3: pH dependence of the observed kinetic parameters for the hydrolysis of L-*p*NA by E151H-AAP. (A) pH dependence of K_m, obtained by subtraction of log(k_{cat}/K_m) from log k_{cat} (—); pK_{e_1} = 6.5, pK_{HS} = 7.6, pK_{e_2} = 10.9, and pK_{e_3} = 11.2. (B) pH dependence of log k_{cat}, fit to the experimental data using eq 4 (—); pK_{ES_1} = 6.4 and pK_{ES_2} = 11.2. (C) pH dependence of log(k_{cat}/K_m), fit to the experimental data using eq 4 (—); pK_{HS} = 7.6 and pK_{e_2} = 10.9. Fits were obtained using Igor Pro (Wavemetrix, Inc., Lake Oswego, OR) and SigmaPlot (SPSS, Inc., Chicago, IL). Error bars are smaller than the symbols used.

at several pH values between 5.5 and 8.0. These data were fit to eq 5, which provided three ionization constants, one for each temperature. A plot of ionization constants versus inverse absolute temperature yields a slope equal to

$$\text{slope} = \Delta H_{ion}/2.303R \qquad (5)$$

where R is the gas constant (Figure 4). The enthalpy of ionization calculated from these data is 3.3 ± 0.3 kcal/mol, more than twice the value expected for a carboxylate group (~1.5 kcal/mol) (*39*) but somewhat lower than typical values for histidine residues (6.9−7.5 kcal/mol).

Solvent Isotope Effect. Solvent isotope effect experiments were carried out at pH 8.50. Proton inventories were obtained by fitting the experimental data to equations derived from the Gross−Butler equation as previously described (*22*). The best fit obtained for E151H-AAP indicated that only one proton is transferred in the rate-limiting step of the reaction at pH 8.50 (Figure 5A). The fit yielded a fractionation factor

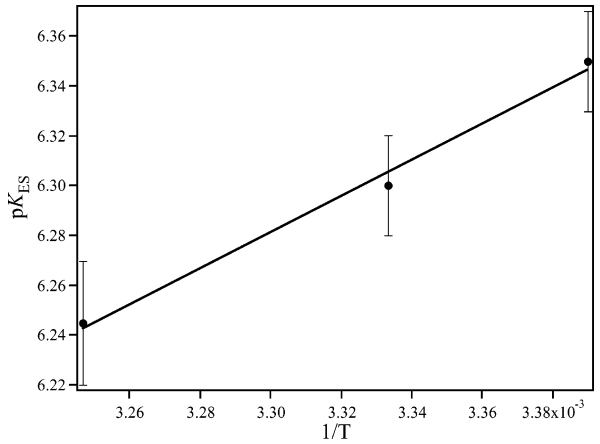

FIGURE 4: Temperature dependence of the ionization constant of the enzyme−substrate complex (pK_{ES_1}). Calculated ΔH_{ion} is 3.3 ± 0.3 kcal/mol.

of 0.42, similar to the fractionation factor found at pH 10.50 for WT-AAP (0.37) (*22*), which was proposed to result from the transfer of a proton to the leaving group of the substrate. The overall kinetic isotope effect is 2.42, which is slightly smaller than that observed for r-AAP at pH 8.00 (2.73) and 20% smaller than that observed for r-AAP or E151D-AAP at pH 10.50 (2.95 and 2.99) (*22*). No changes in K_m were observed in D_2O buffers at a pH/pD of 8.50 (Figure 5B), and a nonunitary value of the solvent isotope effect clearly show that substrate binding is not rate-limiting (*40*).

Spectroscopic Studies. Electronic absorption spectra were recorded for [Co_(E151H-AAP)], [CoCo(E151H-AAP)], and [ZnCo(E151H-AAP)], and the absorbance of the apoprotein was subtracted (Figure 6). Electronic absorption spectra of [Co_(E151H-AAP)] revealed significant changes in both the shape and energy of the observed transitions, with the largest change being observed for the first metal-binding site. Although a transition at approximately 525 nm observed for [Co_(E151H-AAP)] is typical for WT AAP, a broad shoulder was also observed with a λ_{max} of 546 nm. A second, well-defined maximum was observed at 586 nm, with another shoulder at ~625 nm. The addition of a second equivalent of Co^{II} did not change the shape of the observed spectrum but resulted in an increase in the molar absorptivity by 21 M^{-1} cm^{-1} at 522 nm. The addition of Zn^{II} to apo-E151H did not result in any change in the molar absorptivity (ϵ), but the addition of Co^{II} to [Zn_(E151H-AAP)] produced a spectrum very similar to [ZnCo(AAP)] with a molar absorptivity of 19 M^{-1} cm^{-1} at 525 nm.

EPR spectra of the Co^{II}-substituted forms of E151H-AAP were also recorded, and each exhibited an axial $M_S = |\pm 1/2\rangle$ signal, although simulation indicates some rhombicity (E/D = 0.11), consistent with moderate spin−orbit coupling ($g_{x,y}$

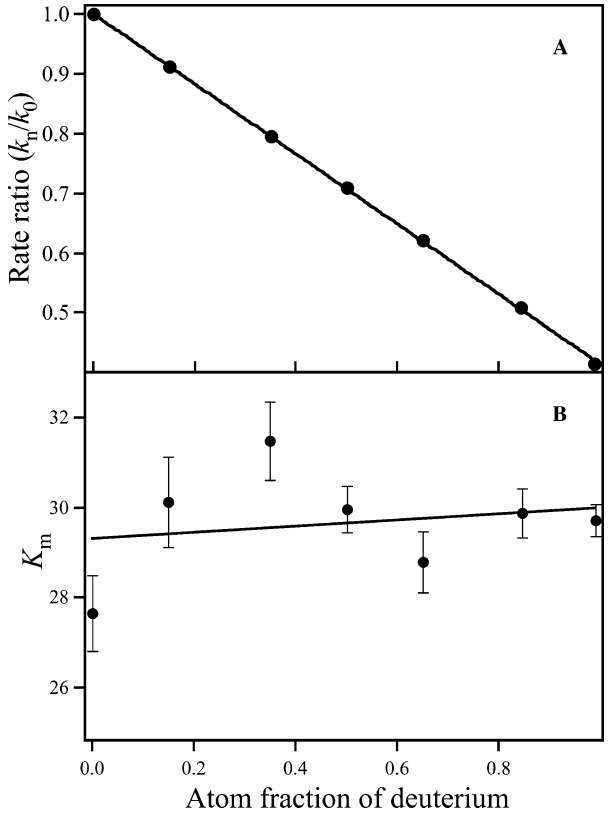

FIGURE 5: (A) Proton inventory of L-*p*NA cleavage by E151H-AAP at pH/pD 8.50. Rate ratio is defined as $k_n/k_{cat,HOH}$, where n is the atom fraction of deuterium. The fractionation factor was obtained by fitting the experimental data to the Gross−Buttler equation (*48*, *56*) and found to be $\phi_T = 0.42$. (B) Dependence of K_m on the atom fraction of deuterium at pH/pD 8.50.

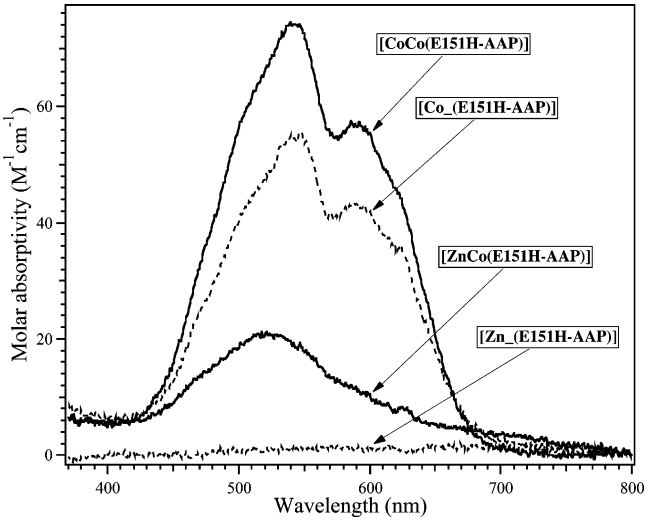

FIGURE 6: UV−vis absorption spectra of E151H-AAP titrated with Co^{II} (from bottom to top: [Zn_(E151H-AAP)], solid line; [ZnCo-(E151H-AAP)], dashed line; [Co_(E151H-AAP)], solid line; and [CoCo(E151H-AAP)], dashed line).

$= 2.42$ and $g_z = 2.45$) (Figure 7). The strong similarity of the observed EPR spectra of [Co_(E151H-AAP)], [ZnCo-(E151H-AAP)], and [CoCo(E151H-AAP)] suggests that these samples both contain appreciable amounts of a common species. A minor species in the EPR spectrum of [Co_(E151H-AAP)] exhibits hyperfine structure ($A_{eff} = 0.011$ cm^{-1} = 103 G), for which only the low-field g value can be resolved with g_{eff} for the visible feature around 8.05.

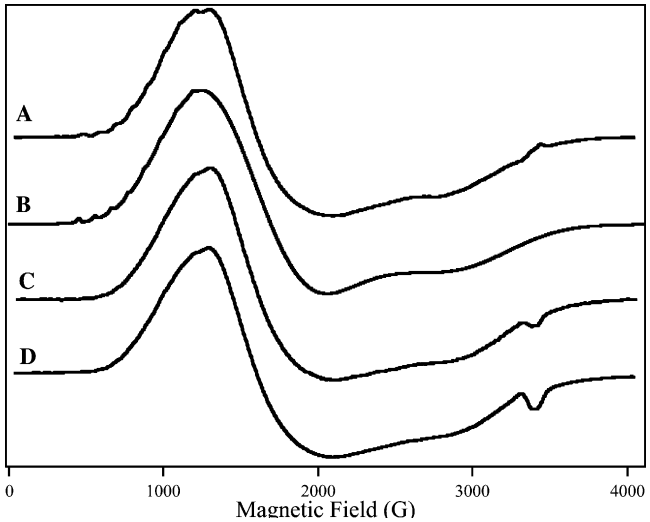

FIGURE 7: EPR spectra of Co^{II}-substituted E151H-AAP. (A) EPR spectrum of [Co_(E151H-AAP)] recorded at 10 K and 0.2 mW microwave power. (B) simulation of spectrum A with $g_{(x,y,z)}$ values of 2.42, 2.42, and 2.45 ($S = {}^3/_2$; $M_S = |\pm{}^1/_2\rangle$). (C) EPR spectrum of [CoCo(E151H-AAP)] recorded at 10 K and 0.2 mW microwave power. (D) EPR spectrum of [ZnCo(E151H-AAP)] recorded at 10 K and 0.2 mW microwave power.

X-ray Structure of E151H-AAP. The X-ray crystal structure of [ZnZn(E151H-AAP)] was solved to 1.9 Å resolution and is shown in Figure 8. Alteration of E151 to histidine does not introduce major conformational changes to the overall protein structure. The structure of [ZnZn(AAP)] and [ZnZn-(E151H-AAP)] agree with a root-mean-square deviation (rmsd) of 0.042 Å for the 291 structurally equivalent Cα atoms. The amino acid residues ligated to the dizinc(II) cluster in E151H-AAP are identical to those in the native structure with only minor perturbations to the bond lengths (Table 3). Zn1 of [ZnZn(E151H-AAP)] exhibits a distorted tetrahedral coordination geometry or a distorted trigonal bipyramidal geometry, with the N^{ϵ} nitrogen of H256 and the bridging water/hydroxide oxygen atom making up the axial positions, if both oxygen atoms if E152 are counted as ligands. Similarly, Zn2 resides in a distorted tetrahedral coordination geometry or a distorted trigonal bipyramidal geometry, with the N^{ϵ} nitrogen of H97 and the bridging water/hydroxide oxygen making up the axial positions, if both oxygen atoms of D179 are counted as ligands. E152 is coordinated in an asymmetric bidentate fashion to Zn1, with the additional oxygen atom providing a potential fifth ligand at a distance of 2.6 Å. Similarly, D179 is coordinated to Zn2 in an asymmetric bidentate fashion, with the second oxygen atom residing 2.6 Å from the metal center providing a potential fifth ligand. The M−M distance for the E151H-AAP is 3.4 Å with water/hydroxide oxygen atom distances of 2.0 and 2.1 Å from Zn1 and Zn2, respectively. A hydrogen bond exist between H151 and the bridging water/hydroxide with a distance of 3.1 Å (Figure 9). Another potentially important hydrogen-bonding interaction is also observed between an oxygen atom of D99 and the N^{δ} nitrogen of H97 (2.9 Å), forming an Asp-His-Zn triad (*41*).

DISCUSSION

Recently, the X-ray crystal structure of DppA was determined at 2.4 Å resolution and revealed that DppA crystallizes as a decamer (*23*). The C-terminal domains are

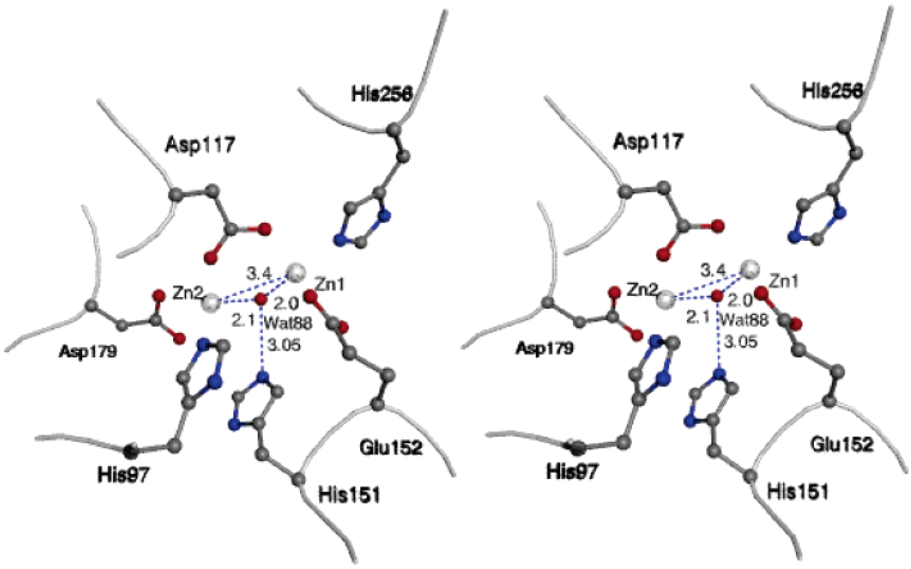

FIGURE 8: Stereoview of the E151H-AAP active site showing Zn1 and Zn2, along with all of the active-site ligands and the bridging water molecule. There is no evidence for bound amino acids or peptides.

Table 3: Selected Bond Lengths (Å) for WT and E151H AAP

	zinc−ligand distance (Å)[a]	
	WT	E151H
Zn1−Zn2	3.5	3.4
Zn1−D117 O2	2.1	2.0
E152 O1	2.0	2.0
E152 O2	2.4	2.6
H256 N2	2.3	2.1
H_2O	2.3	2.0
Zn2−D117 O1	2.0	1.9
D179 O1	2.1	2.1
D179 O2	2.3	2.6
H97 N2	2.3	2.1
H_2O	2.3	2.1
E151 O1	3.4	
H151 N		3.1

[a] The relative error in distance values is ∼0.2 Å.

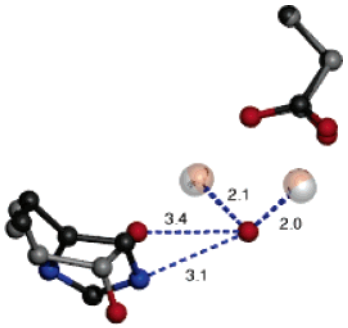

FIGURE 9: Overlay of the active sites of E151H-AAP and WT AAP showing only the Zn1 and Zn2 ions along with E151 (WT) and H151 and the bridging water molecule. The remaining zinc ligands have been removed for clarity. Copper-colored zincs belong to the WT, and the silver-colored zincs belong to E151H.

involved in electrostatic and hydrophobic interactions between the two pentamers in the decamer, whereas the N-terminal domain is responsible for intersubunit contacts between the pentamers (*23*). A cocatalytic Zn^{II}-binding site resides in the N-terminal domain of each monomer, which places them at the center of a 20 Å channel that forms a 50 Å cavity. Similar to AAP, the active site consists of a (μ-aquo)(μ-carboxylato)dizinc(II) core and a Zn−Zn distance of 3.1 Å. The two Zn^{II} ions are coordinated by E10, H60, E133, and H104, with D8 serving as the bridging ligand. Surprisingly, no glutamic acid residue(s) are near the cocatalytic Zn^{II} active site that can function as the general acid/base during catalysis. However, H115 forms a hydrogen bond to the bridging water molecule, suggesting that, in DppA, a histidine residue takes the place of the glutamic acid residues observed in the aminopeptidases AAP and *Streptomyces griseus* (SAP) as well as carboxypeptidase A (CPA) and carboxypeptidase G_2 from *Pseudomonas* sp. strain RS-16 (CPG_2) (*1*, *29*, *35*, *43*, *44*). Unfortunately, no data is available that addresses the role of H115 in the catalytic process of D-amino acid cleavage by DppA. Because the active sites of DppA and AAP are superimposable, glutamate (E151), which functions as the general acid/base during catalytic turnover in AAP (*22*), was altered to a His residue to investigate if a His can function in this capacity in AAP and to serve as a model system for DppA.

Kinetic studies on E151H-AAP revealed a drastic change in catalytic activity. A comparison of the k_{cat} values of E151H-AAP (2.0 min^{-1}) with E151D-AAP (2.4 min^{-1}), E151A-AAP (0 min^{-1}), and r-AAP (4380 min^{-1}), under the same conditions (10 mM borate at pH 8.50 and 0.2 M KCl), reveals that E151 is critical for the catalytic activity of AAP (*22*). Because the activity level of E151H-AAP is ∼2000 times lower than that observed for r-AAP, the metal-binding properties of the E151H altered AAP were investigated via ITC. ITC measurements of Zn^{II} binding to E151H-AAP provided K_d values of 1.0 and 940 μM, for the first and second metal-binding sites, respectively. These values are 330 and 3 times weaker than that observed for WT-AAP. Therefore, H151 perturbs the first metal-binding site more than that of the second Zn^{II}-binding site, but the E151H-AAP enzyme can still bind two divalent metal ions. Interestingly, the Gibbs free energy does not change significantly upon substitution of E151 by histidine and is similar to that observed for r-AAP, E151D-AAP, and E151A-AAP (*53*). Similarly, the entropic factor ($T\Delta S$) remains approximately the same for the first metal-binding event despite a drastic decrease in K_d. However, $T\Delta S$ increases

significantly for the second metal-binding event in the order: E151D < E151H < r-AAP, suggesting a decrease of order around the second metal-binding site.

At pH 8.50, a histidine residue is a better proton shuttle than glutamate because the pK_a of the imidazole ring is closer to pH 8.50 than that of a glutamate, yet E151H-AAP is significantly less active than r-AAP. To address this issue, the pH dependence of the kinetic parameters of [ZnZn-(E151H-AAP)] were examined and revealed a significant change compared to that observed for rAAP and E151D-AAP (*22*). Inspection of a plot of log K_m versus pH revealed a small change in the basic limb of the plot (pK_a = 10.9), suggesting that a tyrosine residue interacts with the substrate (*33*). The small increase in K_m upon substitution of E151 with histidine supports this conclusion and at the same time excludes the possibility of a large rearrangement of the active site. Curvature in the acidic limb provides two inflection points at 6.4 and 7.6. On the basis of previous studies, the latter is assigned to the N-terminal amine of the substrate (L-*p*NA) (*33*). The ionizing group with a pK_a of 6.4 is not observed in pH plots of rAAP and E151D-AAP, suggesting that this ionization is the result of H151. To further determine the identity of this ionizing group, the temperature dependence of k_{cat} was determined. The enthalpy of ionization was found to be 3.3 ± 0.3 kcal/mol, more than twice the value expected for a carboxylate group (~1.5 kcal/mol) (*39*) but approximately half the value typical for histidine residues (6.9−7.5 kcal/mol). This difference may be the result of hydrogen-bond formation between H151 and the bridging water molecule.

Ionizations derived from plots of log(k_{cat}/K_m) versus pH correspond to ionizations of the free enzyme and free substrate (*33*, *39*). A fit of the experimental data to a simple, two-site model, provided two ionization constants: one in the acidic limb at 7.6 that is assigned to the ionization constant of the amino group of the substrate and one in the basic range at 10.9. Interestingly, the most profound difference between the observed pH dependence of E151H-AAP versus rAAP appears in plots of log k_{cat} versus pH, which provided pK_a values of 6.4 and 11.2. The first can be assigned to H151 based on the temperature dependence of the ionization constant of this group as well as a comparison to pH profiles of rAAP and E151D-AAP (*22*). These data strongly support the assignment of the ionizing group observed in the pH profiles of log k_{cat} for rAAP at pH 5.3 to E151 (*22*). The second ionization constant at 11.2, although outside of the pH range used for pH-dependence experiments and thus bearing a large error, was easily reproducible and not present in rAAP or E151D-AAP pH profiles; thus, it is likely for the ionization of the imidazole ring to form a histidinate. The observed pK_a of 11.2 is not significantly different from the pK_a of 13−14, observed for imidazole (*45*). However, on the basis of X-ray crystallographic data and chemical modification studies, this pK_a was previously assigned to Y225 (*33*, *46*). If this pK_a is due to Y225, its catalytic role in E151H-AAP may be the donation of a proton to the $-NH^-$ of the leaving group, because tyrosine is a stronger acid than amine (9.8−10.5 versus ~15). However, Y225 is rather far from the dinuclear metal center (~8 Å) in WT-AAP and thus not a probable proton donor to the leaving group (*35*). To address this proton-transfer process further, proton inventory studies at pH 8.50 were conducted. These data are consistent with one proton being transferred in the rate-limiting step of the reaction at pH 8.5. On the basis of previous studies, this single proton transfer can be assigned to the proton of the general acid (H151) to the leaving group of the substrate (*47*, *48*).

Electronic absorption spectra of the catalytically competent [Co_(E151H-AAP)], [CoCo(E151H-AAP)], and [ZnCo-(E151H-AAP)] enzymes were recorded to gain structural information about the E151H altered AAP enzyme. For a high-spin Co^{II} ion residing in a pentacoordinate field, five transitions from the ground state $^4A'_2$ level to ($^4A''_2$, $^4A''_2$), $^4E''$, $^4E'$, $^4A'_2$(P), and $^4E''$(P) levels are predicted (*49*). Although the molar absorptivity (ϵ) of [Co_(E151H-AAP)] is comparable to [Co_(AAP)] (55 versus 56 M^{-1} cm^{-1}) suggesting a pentacoordinate metal ion for the first metal-binding site, the shape and number of electronic transitions suggest a significant change in geometry (*35*, *50*, *51*). Addition of a second Co^{II} ion to [Co_(E151H-AAP)] results in a small increase in ϵ (~21 M^{-1} cm^{-1}) almost identical to the molar absorptivity increase observed for [ZnCo(E151H-AAP)] (ϵ value of 19 M^{-1} cm^{-1}). The relatively small molar absorptivity increase coupled with the lack of multiple resolved transitions strongly suggests that the second divalent metal-binding site is octahedral, identical to that proposed for WT-AAP (*52*).

EPR spectra of the Co^{II}-substituted forms of E151H-AAP including [ZnCo(E151H)] are intriguing because they are almost indistinguishable and are dominated by a $M_S = |\pm 1/2\rangle$ signal with low rhombicity. The very close similarity between the EPR spectra of [ZnCo(E151H-AAP)], [Co_(E151H-AAP)], and [CoCo(E151H-AAP)] is in marked contrast to the differences between the spectra of [Co_(AAP)], [ZnCo-(AAP)], and [CoCo(AAP)], respectively, and between those of the Co^{II}-substituted forms of the E151 variants of AAP ([Co_(E151A-AAP)] and [CoCo(E151A-AAP)]) (*53*). These comparisons suggest that either the binding mode of E151H differs from that of WT AAP or else the structures of the metal centers, particularly the first metal-binding sites, differ. The X-ray crystal structure of the WT enzyme indicates a distorted tetrahedral of trigonal bipyramidal for Zn_1 and a trigonal bipyramidal geometry for Zn_2 (*35*), whereas electronic absorption and EPR spectroscopies of the Co^{II}-substituted forms are indicative of a five-coordinate Co_1 center and an octahedral Co_2 site. The crystal structure of E151H-AAP suggests that both Zn_1 and Zn_2 reside in trigonal bipyramidal coordination geometries. Interestingly, the EPR and electronic absorption data are most compatible with hexacoordinate Co_1 and Co_2 centers. In fact, examination of another AAP variant, E151D-AAP, also suggested two hexacoordinate Co^{II} ions (*53*). More detailed examination of both the optical and EPR spectra actually suggests a slightly more complex situation, in which Co_1 is in equilibrium between five and six coordinate. The optical absorption spectrum of [Co_(E151A-AAP)] is more intense than that of [ZnCo(E151H-AAP)] by a factor of ~2.5 and contains a structure unexpected for octahedral Co^{II}. Careful examination of the EPR spectrum of [Co_(E151A-AAP)] shows a hyperfine pattern that is significantly diminished in the spectra of [CoCo(E151A-AAP)] and barely discernible in that of [ZnCo(E151A-AAP)]. A full-spin Hamiltonian parameter set cannot be obtained for this signal but it is clear that (i) the strains are very low, suggesting a more con-

strained geometry and/or fewer solvent ligands, and (ii) the rhombic distortion of the axial zero-field splitting is very high. The most likely interpretation of these data is the presence of a five-coordinate species of Co_1, analogous to Zn_1, that is in equilibrium with a predominant six-coordinate species that is formed upon acquisition of a solvent-derived sixth ligand.

Spectroscopic studies suggest that the active site of E151H-AAP still binds two divalent metal ions but that a significant conformational change occurs for site one. However, no detailed information regarding any interaction of H151 within the active site is obtainable from spectroscopic data alone. Therefore, the X-ray crystal structure of E151H-AAP was determined to 1.9 Å resolution (Figure 8). The E151H-AAP structure provides structural information that can be used as a model for DppA. Like all of the structures reported for AAP and its inhibited complexes, a well-defined hydrophobic pocket is adjacent to the dinuclear Zn^{II} active site (*35*, *54*). This hydrophobic pocket has been shown to be the initial substrate recognition and binding point on the enzyme that constitutes the first step in the catalytic mechanism (*55*). Substitution of E151 with a histidine residue does not alter the $Zn^{II}-Zn^{II}$ distance and does not change the coordination number of either Zn^{II}, consistent with the electronic absorption and EPR data. No active-site ligands are displaced upon substitution of E151 with a histidine residue. A bridging water molecule is present between the two Zn^{II} ions, and H151 forms a hydrogen bond with this water molecule, similar to that observed for WT-AAP (Figure 9). H151 presumably can abstract a proton from this water molecule and, on the basis of isotope studies, transfer that proton to the newly formed N-terminal amine group in the transition state, similar to one of the roles of E151 in WT-AAP (*22*).

In conclusion, characterization of E151H-AAP has provided insight into the ability of a histidine residue to function as the general acid/base in hydrolysis reactions of peptides. Although this amino acid has a higher ionization constant than a glutamate, it is still capable of deprotonating the bridging water molecule ($pK_a \sim 7$), thus creating an active-site nucleophile. Through analogy of the role of E151 in AAP, H115 in DppA likely shuttles a proton to the leaving group of the substrate. In addition, pH-dependence studies on E151H-AAP allowed the assignment of an ionizable group in the enzyme−substrate complex of AAP to E151. Significant changes around the geometry and binding of the first metal ion in the active site, combined with kinetic experiments, point to Zn_1, which is coordinated to H256, as the catalytically relevant metal ion.

REFERENCES

1. Holz, R. C., Bzymek, K., and Swierczek, S. I. (2003) Co-catalytic metallopeptidases as pharmaceutical targets, *Cur. Opin. Chem. Biol. 7*, 197.
2. Taylor, A. (1993) Aminopeptidases: Structure and function, *FASEB J. 7*, 290.
3. This reference was deleted during revision.
4. van Moorselaar, R. J., and Voest, E. E. (2002) Angiogenesis in prostate cancer: Its role in disease progression and possible therapeutic approaches, *Mol. Cell. Endocrinol. 197*, 239.
5. Giavazzi, R., and Taraboletti, G. (1999) Angiogenesis and angiogenesis inhibitors in cancer, *Trends Exp. Clin. Med. 9*, 261.
6. D'souza, V. M., Brown, R. S., Bennett, B., and Holz, R. C. (2005) Charaterization of the active site and insight into the binding mode of the anti-angiogenesis agent fumagillin to the Mn^{II}-loaded methionyl aminopeptidase from *Escherichia coli*, *J. Biol. Inorg. Chem. 10*, 41.
7. Passani, L. A., Vonsattel, J. P., Carter, R. E., and Coyle, J. T. (1997) *N*-Acetylaspartylglutamate, *N*-acetylaspartate, and N-acetylated α-linked acidic dipeptidase in human brain and their alterations in Huntington and Alzheimer's diseases, *Mol. Chem. Neuropathol. 31*, 97.
8. Aoyagi, T., Suda, T., Nagai, M., Ogawa, K., Suzuki, J., Takeuchi, T., and Umezawa, H. (1976) Aminopeptidase activities on the surfase of mammalian cells, *Biochim. Biophys. Acta 452*, 131.
9. Pulido-Cejudo, G., Conway, B., Proulx, P., Brown, R., and Izaguirre, C. A. (1997) Bestatin-mediated inhibition of leucine aminopeptidase may hinder HIV infection, *Antiviral Res. 36*, 167.
10. Andoh, T. F., Burdmann, E. A., Lindsley, J., Houghton, D. C., and Bennett, W. M. (1994) Enhancement of Fk506 nephrotoxicity by sodium depletion in an experimental rat model, *Transplantation 57*, 483.
11. Yamada, M., Sukenaga, Y., Fujii, H., Abe, F., and Takeuchi, T. (1994) Purification and characterization of a ubenimex (bestatin)-sensitive aminopeptidase B-like enzyme from K562 human chronic myeloid leukemia cells, *FEBS Lett. 342*, 53.
12. Pulido-Cejudo, G., Conway, B., Proulx, P., Brown, R., and Izaguirre, C. A. (1997) Bestatin-mediated inhibition of leucine aminopeptidase may hinder HIV infection, *Antiviral Res. 36*, 167.
13. Fujii, H., Nakajima, M., Aoyagi, T., and Tsuruo, T. (1996) Inhibition of tumor cell invasion and matrix degradation by aminopeptidase inhibitors, *Biol. Pharm. Bull. 19*, 6.
14. Bradshaw, R., and Yi, E. (2002) Methionine aminopeptidases and angiogenesis, *Essays Biol. Med. 38*, 65.
15. Daiyasua, H., Osakaa, K., Ishinob, Y., and Toha, H. (2001) Expansion of the zinc metallo-hydrolase family of the L-lactamase fold, *FEBS Lett. 503*, 1.
16. Lipscomb, W. N., and Sträter, N. (1996) Recent advances in zinc enzymology, *Chem. Rev. 96*, 2375.
17. Wilcox, D. E. (1996) Binuclear metallohydrolases, *Chem. Rev. 96*, 2435.
18. Dismukes, G. C. (1996) Manganese enzymes with binuclear active sites, *Chem. Rev. 96*, 2909.
19. Barrett, A. J., Rawlings, N. D., and Woessner, J. F. (1998) *Handbook of Proteolytic Enzymes*, pp 1, Academic Press, London, U.K.
20. Chen, G., Edwards, T., D'souza, V. M., and Holz, R. C. (1997) Mechanistic studies on the aminopeptidase from *Aeromonas proteolytica*: A two-metal ion mechanism for peptide hydrolysis, *Biochemistry 36*, 4278.
21. Stamper, C., Bennett, B., Edwards, T., Holz, R. C., Ringe, D., and Petsko, G. (2001) Inhibition of the aminopeptidase from *Aeromonas proteolytica* by L-leucinephosphonic acid. Spectroscopic and crystallographic characterization of the transition state of peptide hydrolysis, *Biochemistry 40*, 7035.
22. Bzymek, K. P., and Holz, R. C. (2004) The catalytic role of glutamate-151 in the leucine aminopeptidase from *Aeromonas proteolytica*, *J. Biol. Chem. 279*, 31018.
23. Remaut, H., Bompard-Gilles, C., Goffin, C., Frere, J. M., and van Beeumen, J. (2001) Structure of the *Bacillus subtilis* D-aminopeptidase DppA reveals a novel self-compartmentalizing protease, *Nat. Struct. Biol. 8*, 674.
24. Desmarais, W., Bienvenue, L. D., Bzymek, K. P., Holz, R. C., Petsko, A. G., and Ringe, D. (2002) The 1.2 Å resolution crystal structure of the aminopeptidase from *Aeromonas proteolytica* complexed with Tris: A tale of buffer inhibition, *Structure*, 1063.
25. Mathiopoulos, C., Mueller, J. P., Slack, F. J., Murphy, C. G., Patankar, S., Bukusoglu, G., and Sonenshein, A. L. (1991) A *Bacillus subtilis* dipeptide transport system expressed early during sporulation, *Mol. Microbiol. 5*, 1903.
26. Cheggour, A., Fanuel, L., Duez, C., Joris, B., Bouillenne, F., Devreese, B., van Driessche, G., van Beeumen, J., Frere, J.-M., and Goffin, C. (2000) The DppA gene of *Bacillus subtilis* encodes a new D-aminopeptidase.
27. Bienvenue, D. L., Gilner, D. M., Davis, R. S., Bennett, B., and Holz, R. C. (2003) Substrate specificity, metal binding properties, and spectroscopic characterization of the DapE-encoded-*N*-succinyl-L,L-diaminopimelic acid desuccinylase from *Haemophilus influenzae*, *Biochemistry 42*, 10756.
28. Javid-Majd, F., and Blanchard, J. S. (2000) Mechanistic analysis of the argE-encoded *N*-acetylornithine deacetylase, *Biochemistry 39*, 1285.

29. Holz, R. C. (2002) The aminopeptidase from *Aeromonas proteolytica*: Structure and mechanism of co-catalytic metal centers involved in peptide hydrolysis, *Coord. Chem. Rev. 232*, 5.
30. Zhang, Z.-Z., Nirasawa, S., Nakajima, Y., Yoshida, M., and Hayashi, K. (2000) Function of the N-terminal propetide of an aminopeptidase from *Vibrio proteolytica*, *Biochem. J. 350*, 671.
31. Prescott, J. M., and Wilkes, S. H. (1976) *Aeromonas* aminopeptidase, *Methods Enzymol. 45*, 530.
32. Prescott, J. M., Wilkes, S. H., Wagner, F. W., and Wilson, K. J. (1971) *Aeromonas* aminopeptidase. Improved isolation and some physical properties, *J. Biol. Chem. 246*, 1756.
33. Baker, J. O., and Prescott, J. M. (1983) *Aeromonas* aminopeptidase: pH dependence and a transition-state-analogue inhibitor, *Biochemistry 22*, 5322.
34. Griffin, M., Muys, A., Noble, C., Wang, D., Eldershaw, C., Gates, K. E., Burrage, K., and Hanson, G. R. (1999) Xsophe, a computer simulation software suite for the analysis of electron paramagnetic resonance spectra, *Mol. Phys. Rep. 26*, 60.
35. Chevrier, B., Schalk, C., D'Orchymont, H., Rondeau, J.-M., Moras, D., and Tarnus, C. (1994) Crystal structure of *Aeromonas proteolytica* aminopeptidase: A prototypical member of the co-catalytic zinc enzyme family, *Structure 2*, 283.
36. Otwinowski, Z., and Minor, W. (1997) Hkl X-ray methods, *Methods Enzymol. 276*, 307.
37. Brünger, A. T. (1997) *X-Plor, a System for X-Ray Crystallography and NMR*, Yale University Press, New Haven, CT.
38. Kabsch, W. (1998) Evaluation of single-crystal X-ray diffraction data from a position-sensitive detector, *J. Appl. Crystallogr. 21*, 916.
39. Segel, I. H. (1993) Enzyme kinetics. Behavior and analysis of rapid equilibrium and steady-state enzyme systems, *Enzyme Kinetics. Behavior and Analysis of Rapid Equilibrium and Steady-State Enzyme Systems*, John Wiley and Sons, Inc., New York.
40. Hegde, S. S., Javid-Majd, F., and Blanchard, J. S. (2001) Overexpression and mechanistic analysis of chromosomally encoded aminoglycoside 2′-*N*-acetyltransferase (Aac(2′)-Ic) from *Mycobacterium tuberculosis*, *J. Biol. Chem.* 45876.
41. Christianson, D. W., and Alexander, R. S. (1989) Carboxylate−histidine−zinc interactions in protein structure and function, *J. Am. Chem. Soc. 111*, 6412.
42. This reference was deleted during revision.
43. Greenblatt, H. M., Almog, O., Maras, B., Spungin-Bialik, A., Barra, D., Blumberg, S., and Shoham, G. (1997) *Streptomyces griseus* aminopeptidase: X-ray crystallographic structure at 1.5 Å resolution, *J. Mol. Biol. 265*, 620.
44. Christianson, D. W., and Lipscomb, W. N. (1989) Carboxypeptidase A, *Acc. Chem. Res. 22*, 62.
45. Martin, R. B. (1974) Pyrrole hydrogen ionization of imidazole derivatives in metal ion complexes and carbonic anhydrase, *71*, 4346.
46. Makinen, K. K., Makinen, P. L., Wilkes, S. H., Bayliss, M. E., and Prescott, J. M. (1982) Chemical modification of *Aeromonas* aminopeptidase. Evidence for the involvement of tyrosyl and carboxyl groups in the activity of the enzyme, *Eur. J. Biochem. 128*, 257.
47. Schowen, K. B., and Schowen, R. L. (1982) Solvent isotope effects of enzyme systems, *Methods Enzymol. 87*, 551.
48. Venkatasubban, K. S., and Schowen, R. L. (1984) The proton inventory technique, *CRC Crit. Rev. Biochem. 17*, 1.
49. Lever, A. B. P. (1984) Inorganic electronic spectroscopy, *Inorganic Electronic Spectroscopy*, 2nd ed., Vol. 33, Elsevier, New York.
50. Bennett, B., and Holz, R. C. (1997) EPR studies on the mono- and dicobalt(II)-substituted forms of the aminopeptidase from *Aeromonas proteolytica*. Insight into the catalytic mechanism of dinuclear hydrolases, *J. Am. Chem. Soc. 119*, 1923.
51. Bennett, B., and Holz, R. C. (1997) Spectroscopically distinct cobalt(II) sites in heterodimetallic forms of the aminopeptidase from *Aeromonas proteolytica*: Characterization of substrate binding, *Biochemistry 36*, 9837.
52. Prescott, J. M., Wagner, F. W., Holmquist, B., and Vallee, B. L. (1985) Spectral and kinetic studies of metal-substituted *Aeromonas* aminopeptidase: Nonidentical, interacting metal-binding sites, *Biochemistry 24*, 5350.
53. Bzymek, K. P., Swierczek, S. I., Bennett, B., and Holz, R. C. (2005) Spectroscopic characterization of the E151d and E151a altered aminopeptidases from *Aeromonas proteolytica*, *Inorg. Chem.*, manuscript submitted.
54. Chevrier, B., D'Orchymont, H., Schalk, C., Tarnus, C., and Moras, D. (1996) The structure of the *Aeromonas proteolytica* aminopeptidase complexed with a hydroxamate inhibitor. Involvement in catalysis of Glu151 and two zinc ions of the cocatalytic unit, *Eur. J. Biochem. 237*, 393.
55. Ustynyuk, L., Bennett, B., Edwards, T., and Holz, R. C. (1999) Inhibition of the aminopeptidase from *Aeromonas proteolytica* by aliphatic alcholols. Characterization of the hydrophobic substrate recognition site, *Biochemistry 38*, 11433.
56. Albery, W. J. (1975) Proton transfer reactions, *Proton-Transfer Reactions*, Chapman and Hall, London, U.K. Venkatasubban, K. S., and Schowen, R. L. (1984) The proton inventory technique, *CRC Crit. Rev. Biochem. 17*, 1.

BI0505823